

Source of Gravity Waves within a Vortex-Dipole Jet Revealed by a Linear Model

SHUGUANG WANG*

Department of Atmospheric Sciences, Texas A&M University, College Station, Texas

FUQING ZHANG

Department of Meteorology, The Pennsylvania State University, University Park, Pennsylvania

(Manuscript received 21 September 2009, in final form 18 January 2010)

ABSTRACT

This study develops a linear numerical model to address the source mechanism of the gravity waves generated within a vortex dipole simulated in a fully nonlinear nonhydrostatic mesoscale model. The background flow for this linear model is obtained from potential vorticity inversion constrained by the nonlinear balance equation. The forcing imposed in the linear model is derived from an imbalance in the large-scale flow—that is, the forcing or imbalance in the vorticity, divergence, and thermodynamic equations, respectively. The response from the sum of these imbalanced forcings obtained from the linear dynamics shows well-defined gravity wave signals, which compare reasonably well in terms of location, phase, and amplitude with the gravity waves simulated in a fully nonlinear nonhydrostatic mesoscale model. It is found that the vorticity forcing, largely due to the advection of balanced relative vorticity, is the leading contributor to the gravity waves in the exit region of the vortex-dipole jet.

1. Introduction

Atmospheric jets are known to generate gravity waves. Gravity wave emission in the exit region of jets has been documented in many studies, such as those based on observations (e.g., Uccellini and Koch 1987; Koch and Dorian 1988; Schneider 1990; Hertzog et al. 2001; Zhang et al. 2001; Plougonven and Teitelbaum 2003; Wu and Zhang 2004; Koch et al. 2005) and on numerical simulations of gravity waves within baroclinic life cycles (O’Sullivan and Dunkerton 1995; Zhang 2004; Wang and Zhang 2007; Plougonven and Snyder 2007).

Different hypotheses have been proposed in previous studies for the generation of gravity waves from jets. Geostrophic adjustment—the radiation of gravity waves through adjusting the imbalance between wind and mass fields (Rossby 1938; Cahn 1945; Blumen 1972; Fritts and

Luo 1992; Luo and Fritts 1993)—is believed to be responsible for gravity wave generation in Kaplan and Paine (1977), Van Tuyl and Young (1982), and Uccellini and Koch (1987). Various diagnostic tools of flow imbalance that leads to geostrophic adjustment have been used in the past (e.g., O’Sullivan and Dunkerton 1995; Koch and Dorian 1988; Zhang et al. 2000; Plougonven et al. 2003). Among these tools, the residual of the nonlinear balance equation (Δ NBE) is frequently used to examine flow imbalance near upper-level jets. Zhang (2004) illustrates that Δ NBE as well as gravity waves are both continuously generated in the exit region of a baroclinic jet. He further proposed that balance adjustment, as a generalization of geostrophic adjustment, is responsible for gravity wave generation in the jet in which gravity waves are continuously forced by flow imbalance while the developing background baroclinic waves are continuously producing flow imbalance that needs to be adjusted. The spontaneous balance adjustment hypothesis is further elaborated by Plougonven and Zhang (2007, hereafter PZ07) based on scale analysis by rearranging equations such that small-scale components are governed by linear dynamics with forcing from imbalance in the primary large-scale flow on the right-hand side. In a related approach, in the study of wave generation

* Current affiliation: Department of Applied Physics and Applied Mathematics, Columbia University, New York, New York.

Corresponding author address: Dr. Fuqing Zhang, Department of Meteorology, The Pennsylvania State University, University Park, PA 16802.
E-mail: fzhang@psu.edu

from frontogenesis, Snyder et al. (1993) suggest that gravity waves may be spontaneously generated owing to “residual tendencies,” that are essentially an imbalance between fields that are in balance in the balanced dynamics but otherwise unbalanced in the fully nonlinear primitive equation dynamics.

Recently, gravity waves from vortex dipoles have been examined in great detail (Viúdez 2006, 2007, 2008; Snyder et al. 2007, 2009; McIntyre 2009; Wang et al. 2009). In this highly idealized framework, inertia–gravity waves appear in the exit region of the localized jet and maintain coherent structures within the moving frame of vortex dipoles on time scales of many inertial periods. These waves have a relatively low intrinsic frequency of one to two times the Coriolis parameter and a characteristic horizontal scale of several hundreds of kilometers. Because such a spatial scale is smaller than the scale of the vortex motion, it is questionable to directly apply the theory of shallow-water spontaneous wave emission (Plougonven et al. 2009; Ford 1994; Ford et al. 2000), which was developed under the assumption that the spontaneously emitted waves have much larger spatial scales than their sources. Using a linearized version of the primitive equation model, Snyder et al. (2009) demonstrate that these waves are a forced, linear response owing to the residual tendency of the balanced flow. Viúdez (2007) suggests that these wave packets originate from the large acceleration of the fluid particles as they move along the anticyclonic side of the dipole axis, but he did not directly solve for the wave response forced by the particle acceleration.

The present study attempts to further investigate wave generation from vortex-dipole jets. Here we follow the basic framework proposed in PZ07 but linearize the wave equation based on a nonlinearly balanced background state. The balanced background state is obtained through potential vorticity (PV) inversion constrained with a nonlinear balanced equation, which avoids the ambiguity in the scale separation in PZ07. We seek to compare the forced response to the nonlinear model solutions and thus provide clear evidence for the wave generation as the forced response, to compare wave response from different sources (the divergent, vorticity, and thermodynamic sources) that are identified in PZ07 and to examine the effectiveness of using flow imbalance diagnosed from ΔNBE as a wave precursor under the linear framework.

Based on these linearized equations, a linearized numerical model is developed to further study the generation of gravity waves from a localized jet within the vortex-dipole jet simulated in Wang et al. (2009). A linear model similar to, but independent from, the current study is recently reported in Snyder et al. (2009),

which also examines the source mechanism of gravity waves in the vortex dipoles simulated in Snyder et al. (2007).

The current study complements and expands the study of Snyder et al. (2009) in that 1) we employ the potential vorticity inversion based on the nonlinear balance equation to obtain the balanced flow, thus avoiding the systematic bias in the quasigeostrophic (QG) dynamic relative to the fully nonlinear dynamics; 2) our linearized model formulation allows direct partition of wave sources from imbalance in the vorticity, divergence, and thermodynamic equations; 3) the formulation of our linearized model allows us to identify directly the source of the linear instability found in Snyder et al. (2009); and 4) our analysis focuses on the gravity wave generation from a midtropospheric vortex-dipole jet in Wang et al. (2009) rather than from the surface-trapped vortex dipoles as in Snyder et al. (2007, 2009).

The rest of this article is organized as follows. Section 2 reviews the nonlinear model-simulated gravity waves. Diagnostics of the forcing to the linear model is presented in section 3. Section 4 discusses the results from both the complete linear model and a simplified linear model in which shear terms are neglected. The wave response to the forcing diagnosed from the balanced fields is discussed in detail using the simplified linear model. The robustness of the wave solution is examined through sensitivity experiments in section 5. Comparison of the wave response from the current linear work to that proposed in PZ07 is given in section 6. Concluding remarks are presented in section 7.

2. Review of gravity waves in a vortex dipole simulated using a mesoscale model

The localized jet within the middle-level vortex dipoles is adopted from the simulation in Wang et al. (2009) in which a nonhydrostatic compressible mesoscale modeling system [the fifth-generation Pennsylvania State University–National Center for Atmospheric Research Mesoscale Model (MM5)] is used. The quasi-balanced vortex dipole is slowly translating at a speed of $\sim 1.1 \text{ m s}^{-1}$ during a time period of 25 days. Figure 1 shows the gravity wave signature in the horizontal wind divergence (Figs. 1a,b) and vertical velocity (Figs. 1c,d) at 210 h. There is an ascent/descent couplet above and below the level of the maximum wind ($\sim 11.5 \text{ km}$), which has been noted by Viúdez (2007) and Snyder et al. (2007). Viúdez recovered this low-wavenumber couplet by inverting the generalized omega equation and concluded that this is responsible for wave generation. He further concluded that the origin of this ascent/descent couplet is the material rate of change of the ageostrophic differential vorticity.

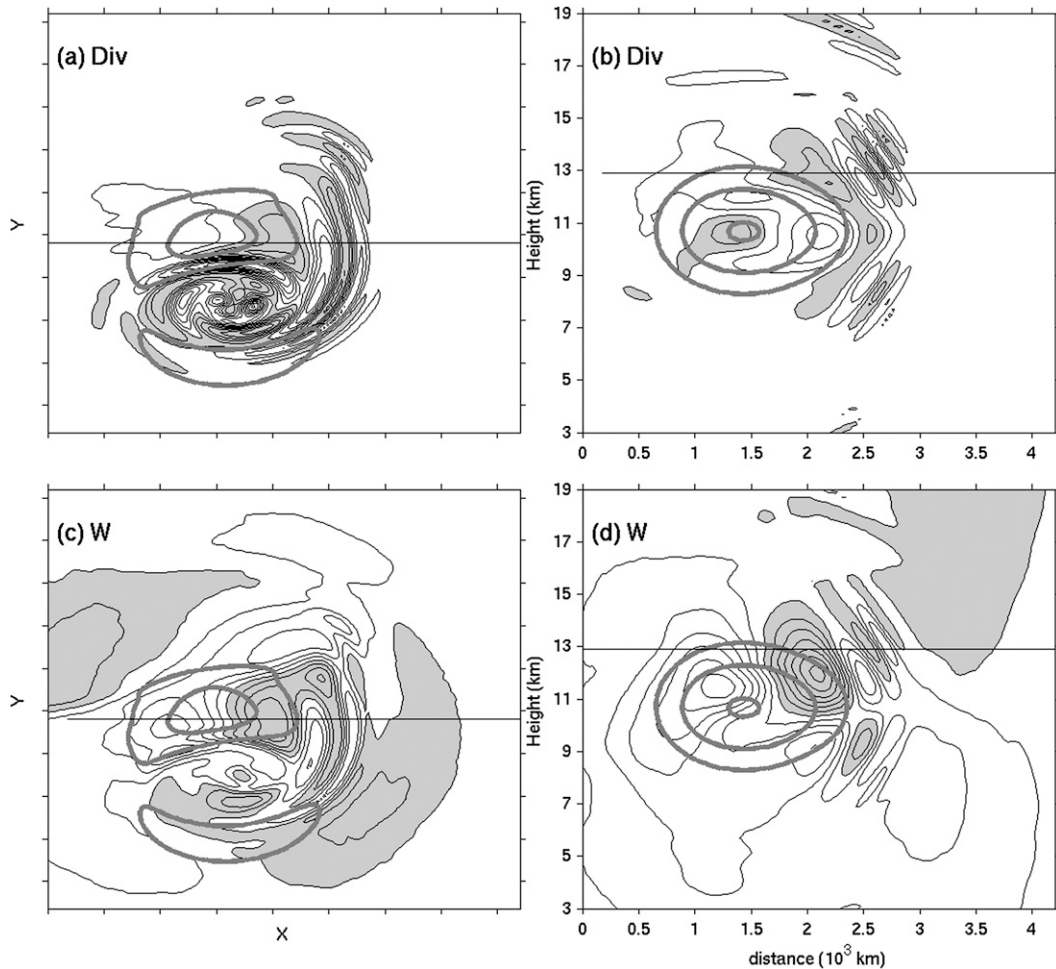


FIG. 1. The MM5 simulated horizontal divergence [contour interval (CI) = $1 \times 10^{-6} \text{ s}^{-1}$; zero value omitted; shaded, positive] (a) at 12.9 km and (b) the corresponding vertical cross section at 210 h. (c),(d) As in (a),(b) but for the vertical velocity (CI = $5 \times 10^{-4} \text{ m s}^{-1}$; zero value omitted; shaded, positive). Wind speed (thick gray) is contoured at 20, 25, and 30 m s^{-1} at 11.5 km in (a) and (c), and along the vertical cross sections in (b) and (d). The solid gray lines in (a) and (c) indicate the cross sections in (b) and (d). The solid gray lines in (b) and (d) indicate the level of 12.9 km. Distance between ticks in (a) and (c) is 500 km.

In the following section, it will be shown that our linear model can also reproduce this ascent/descent couplet as nonpropagating waves.

3. Forcing diagnosed from the balanced flow

PZ07 derived the governing linear dynamics with the forcing from the large-scale primary flow. The divergence, vorticity, and thermodynamic forcing terms F_δ , F_ζ , and F_θ are defined as

$$\begin{aligned} F_\delta &= \partial_x F_u + \partial_y F_v, \\ F_\zeta &= \partial_x F_v - \partial_y F_u, \\ F_\theta &= -(\partial_t + \mathbf{U}_B \cdot \nabla) \theta_B - w_B \partial_z \bar{\Theta}, \end{aligned} \quad (1)$$

where $\mathbf{U} = (u, v, w)$ are three wind components, θ the potential temperature, and $\bar{\Theta}$ the reference potential temperature. Subscript B denotes the balanced, large-scale flow, which is also termed the background flow or the primary flow in later sections. Here F_u and F_v are defined as

$$\begin{aligned} F_u &= -(\partial_t + \mathbf{U}_B \cdot \nabla) u_B + f v_B - \partial_x \Phi_B, \\ F_v &= -(\partial_t + \mathbf{U}_B \cdot \nabla) v_B - f u_B - \partial_y \Phi_B, \end{aligned}$$

where δ is the horizontal divergence, ζ the vertical relative vorticity, Φ the Boussinesq disturbance pressure, and f the constant Coriolis parameter. These forcing terms are not directly interpreted as the forcing to gravity waves; rather, they are forcing to linear dynamics that projects to the wave modes since the linear dynamics may

also project to the balanced motion (Plougonven et al. 2009). Note that these forcing terms are similar to the “residual tendencies” used in Snyder et al. (2009) in the sense that they are evaluated using the fields that are in balance in the balanced dynamics but otherwise unbalanced in the full nonlinear dynamics.

Instead of using a quasigeostrophically balanced background state as in Snyder et al. (2009), the current study uses the balanced flow derived from potential vorticity inversion under the constraint of nonlinear balance (Davis and Emanuel 1991), which eliminates gravity waves and imbalance imbedded in the total flow. The nonlinear balance has higher-order accuracy than quasigeostrophy and is applicable at both synoptic scale and mesoscale (Gent and McWilliams 1982; Zhang et al. 2000). The current linearization is also different from PZ07 in that they made no assumption on the balance of the primary flow in their scaling analysis and thus left open the definition of the separation between balance and imbalance or gravity waves.

It is straightforward to obtain balanced variables such as horizontal winds, pressure, and potential temperature through PV inversion except for the balanced vertical velocity w . In this study, the vertical velocity in the large-scale balanced flow is approximated by the QG vertical velocity. As we show later, our forced wave solution is not sensitive to this approximation; also there is only marginal difference in the solution when zero vertical velocity is used for the forcing calculation.

Figure 2 shows the distribution of these forcing terms that are computed from the balanced approximation to the raw 30-km MM5 solution valid at 210 h. The time tendency of large-scale flow ($\partial_t u_B$, $\partial_t v_B$, $\partial_t \theta_B$) in Eq. (1) has been dropped because the characteristic time scale of the large-scale flow is much larger than that of the disturbance and because these time tendency terms are much smaller than the other terms. The forcing terms in Fig. 2 have been smoothed by a 2D digital filter with a cutoff wavelength 600 km. Nevertheless, F_δ in Figs. 2a,b does not have the localized structure as ΔNBE (Fig. 6 in Wang et al. 2009, also Fig. 10) because ΔNBE is everywhere zero, as implied in the nonlinearly balanced state. Also, no apparent localized or compact structures are found in F_θ (Figs. 2e,f) near the jet core. Among the three forcing terms, only the vorticity forcing F_ζ (Fig. 2d) has a compact region with negative values between 9 and 11 km near the jet core.

To gain further insight from the diagnosed forcing above, let the wave operator be implicitly written as

$$L(w') = G_\delta + G_\zeta + G_\theta, \quad (2)$$

where $L(w')$ is the linear operator and w' the perturbation vertical velocity. The operator $L(w')$ can be written,

if all the cross derivatives of basic flow quantities are neglected as in PZ07, as

$$L(w') = \{[(\partial_t + \mathbf{U}_B \cdot \nabla)^2 + f^2]\partial_{zz} + N^2\Delta_H\}w', \quad (3)$$

where Δ_H is the horizontal Laplacian. In the flow with constant background winds, this operator $L(w')$ yields a standard gravity wave dispersion relationship. Here G_δ , G_θ , and G_ζ are

$$G_\delta = -(\partial_t + \mathbf{U}_B \cdot \nabla)\frac{\partial F_\delta}{\partial z}; \quad G_\zeta = -f\frac{\partial F_\zeta}{\partial z}; \quad G_\theta = \frac{g}{\Theta}\Delta F_\theta. \quad (4)$$

Under the linear assumption, the total response is the sum of all the individual response to the transformed forcing F_δ , F_ζ , or F_θ ; that is, G_δ , G_θ , and G_ζ . These terms are named *normalized forcing*. The normalized forcing terms emphasize that regions potentially important for wave generation are those having large values of either the Lagrangian derivative of the vertical gradient of the divergence forcing F_δ or vertical gradient of the vorticity forcing F_ζ or the Laplacian of the thermal forcing F_θ . Thus the linear wave operator (3) implies that imbalance in fully nonlinear dynamics among terms that consist of balanced quantities is a possible source of gravity waves, if forcing is projected onto wave modes. Note that the linear wave operator includes the balanced flow \mathbf{U}_B . This has important consequences: the wave packets feel the wind shear along their propagation, their spatial scales and frequency are strongly constrained, and their energy is concentrated, as demonstrated through experiments with prescribed forcing with different horizontal and vertical scales in Wang et al. (2009, manuscript submitted to *Quart. J. Roy. Meteor. Soc.*).

Equations (2)–(4) are similar to Eq. (15) in PZ07, but the current formulation does not assume the importance of the leading terms as identified in PZ07 through scaling argument since the balanced flow from PV inversion, instead of the total flow directly from nonlinear simulations, is used in evaluating the forcing terms. This also has important implications for calculating the divergence forcing term: since the residual of nonlinear balance equation is constrained to be zero for PV inversion, ΔNBE , the lead term in the divergence forcing of PZ07 now disappears. Comparison of wave response from the current linear model with that of PZ07 will be presented in section 6.

Our approach to obtain the solution of Eq. (2) is to time integrate Eqs. (A1.1)–(A1.5) (see the appendix) with imposed forcing in Eq. (1) to a steady state. We obtain instantaneous balanced fields through inverting PV from the full nonlinear model simulation under

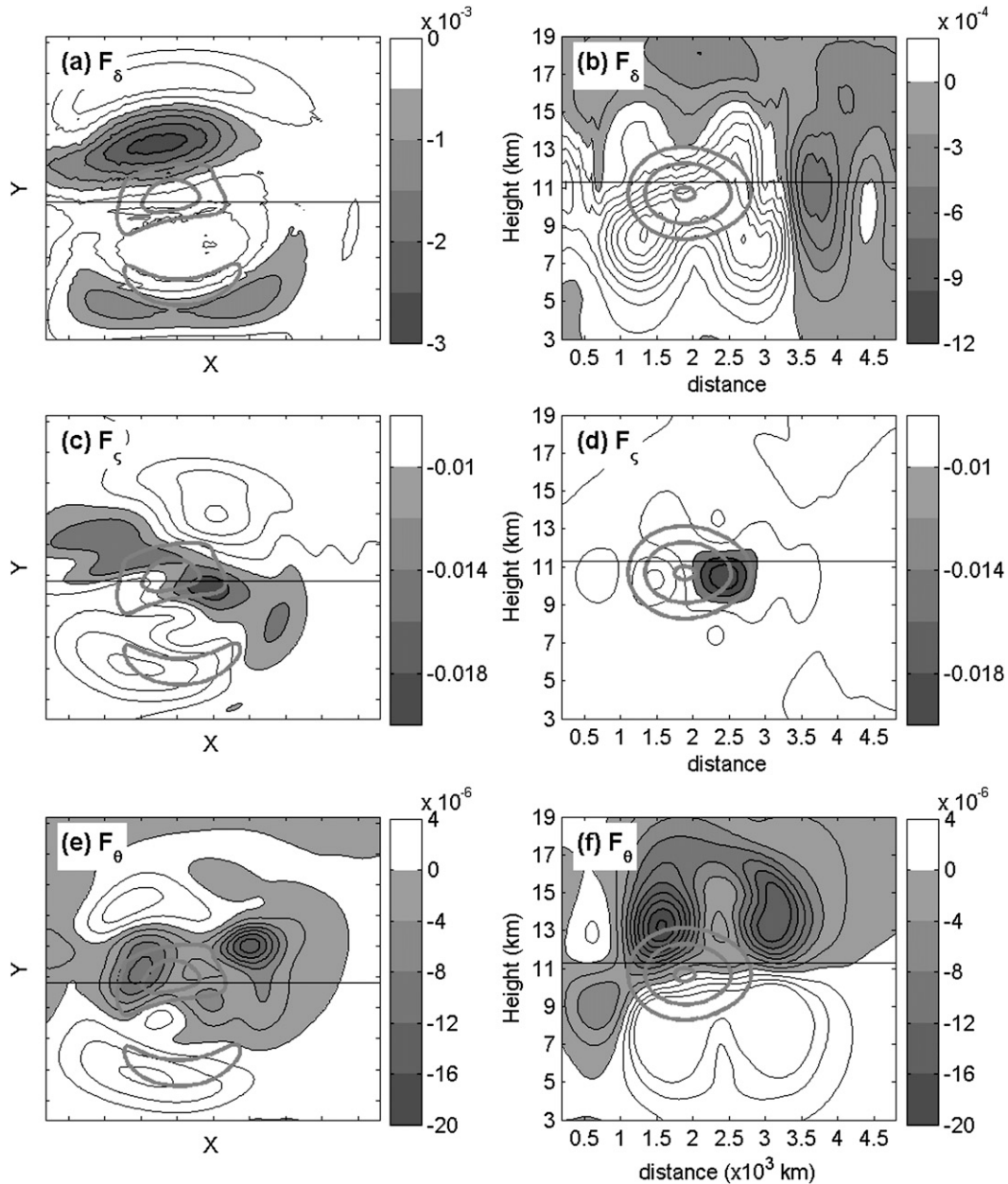


FIG. 2. The forcing term F_δ (a) at 11.3 km ($CI = 5 \times 10^{-12} \text{ m s}^{-2}$) and (b) along the vertical cross section ($CI = 1 \times 10^{-12} \text{ m s}^{-2}$). (c),(d) As in (a),(b) but for F_ζ ($CI = 5 \times 10^{-11} \text{ m s}^{-2}$). (e),(f) As in (a),(b) but for F_θ ($CI = 2 \times 10^{-7} \text{ K s}^{-1}$). Wind speed (thick gray) is contoured at 20, 25, and 30 m s^{-1} at 11.5 km in (a),(c), and (e) and along the vertical cross sections in (b),(d) and (f). The solid gray lines in (a),(c), and (e) indicate the cross sections in (b),(d), and (f), respectively. The solid gray lines in (b),(d), and (f) indicate the level of 11.3 km. The distance between ticks in (a),(c), and (e) is 500 km.

the nonlinear balance condition. In general, the nonlinearly balanced flow is a better approximation to the nonlinear dynamics than the QG approximation. Snyder et al. (2009) use an independent filtered dynamical model (a QG model) to approximate the balanced flow and evaluate their forcing terms. There is a systematic phase bias using a time-evolving filtered dynamic

model relative to the full nonlinear solution. Such a bias may lead to the breakdown of the linear assumption in a few days, which will be avoided in this current study.

Figure 3 shows these G terms and their sum $G_\delta + G_\theta + G_\zeta$. Among the three normalized forcing terms, G_ζ has the maximum amplitude, $0.1 \times 10^{-16} \text{ m}^{-1} \text{ s}^{-3}$, while

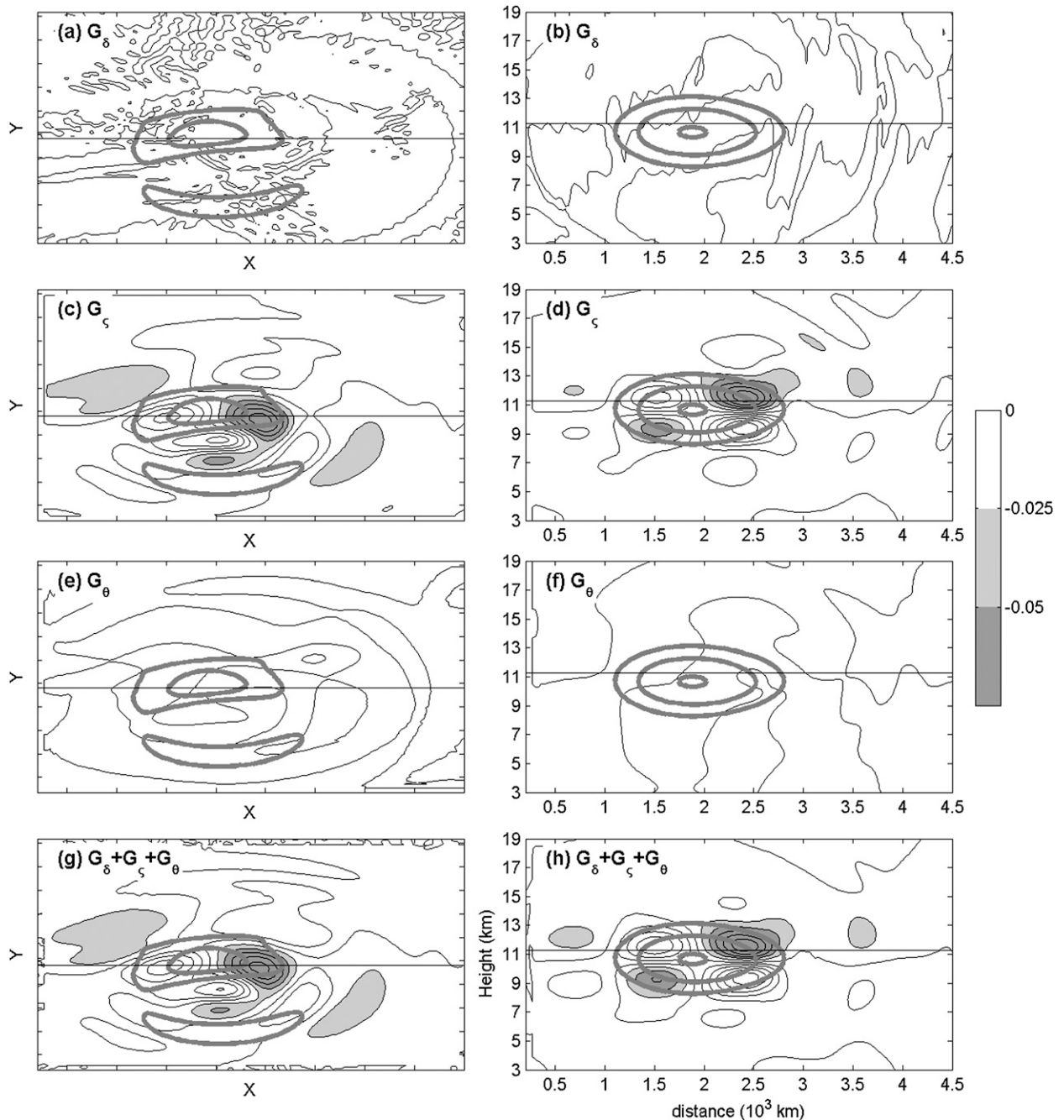


FIG. 3. The normalized forcing terms G_δ , G_θ , G_ζ , and (left column) their sum at 11.3 km and (right column) vertical planes. All fields have the same contour interval: $0.025 \times 10^{-16} \text{ m}^{-1} \text{ s}^{-2}$. Wind speed (thick gray) is contoured at 20, 25, and 30 m s^{-1} (left) at 11.5 km and (right) along the vertical cross sections. The solid gray lines (left panels) indicate the cross sections (right panels). The solid gray lines in (b),(d),(f), and (h) indicate the level of 11.3 km. The distance between ticks (left panels) is 500 km.

other terms are much smaller. The sum of these three terms $G_\delta + G_\theta + G_\zeta$, similar to G_ζ , reveals a clear compact structure with a quadruple pattern concentrated near the jet core. The importance of each forcing term in wave generation within the vortex dipole will be examined in the next section.

4. Linear responses obtained using the linear model

a. Numerics of the linear model

The nonhydrostatic, compressible linear model is documented in Wang et al. (2009, manuscript submitted to *Quart. J. Roy. Meteor. Soc.*). The prognostic variables of

the model are the following perturbation variables: horizontal divergence, vorticity, Boussinesq disturbance pressure, potential temperature, and vertical velocity (see the formulation in the appendix). It uses height as the vertical coordinate. For the sake of both numerical accuracy and efficiency, the model marches the perturbation variables using a time-splitting scheme: the large time step uses a Runge–Kutta third-order scheme (Wicker and Skamarock 2002) and the small time step handles fast propagating acoustic waves (Klemp and Wilhelmson 1978; Skamarock and Klemp 1992). In all the linear model simulations discussed below, the horizontal (vertical) grid spacing is 30 km (200 m), the same resolution as the fully nonlinear MM5 simulation. Sponge layers are used near the top, bottom, and lateral boundaries with the maximum Rayleigh damping coefficient of 10^{-5} s^{-1} . The sponge layer is 3 km deep near the bottom and top boundaries and 450 km wide near the lateral boundaries. The fourth-order horizontal filter has a coefficient of $10^{-2} Dx^4/Dt$, where Dx is the grid size and Dt is the time step.

The linear model runs either with or without all the shear terms involving the derivatives of balanced quantities [the braces and brackets in Eqs. (A1.1)–(A1.5)]. As shown below, linear instability is found in the full linear model with these shear terms included. On the other hand, a quasi-stationary wave response can also be obtained with the shear terms neglected. We also apply Newtonian cooling with a coefficient of $5.5 \times 10^{-7} \text{ s}^{-1}$ (500 h). The spatial structure barely changes after 200 h.

b. Response of the simplified linear model to the diagnosed forcing

Here we use a simplified version of the linear model to study wave response. We neglect the terms associated with the advection of primary flow by disturbance winds [the braces and brackets in Eqs. (A1.1)–(A1.5); e.g., $\mathbf{u}' \cdot \nabla \mathbf{u}_B$]. This simplification practically eliminates the possible instability in the dipole flow, as discussed in the next subsection. This simplification can partly be justified by the commonly used WKB approximation (e.g., Marks and Eckermann 1995).

Figure 4 displays the linear response due to the forcing terms F_δ , F_θ , and F_ζ from the simplified linear model (Fig. 2). A well-defined wave pattern from the vortex-dipole jet is found in the linear solution. Specifically, the wave pattern in the horizontal plane at 12.9 km shows a spiral pattern with most wave energy focused on the anticyclonic side of the dipole. In the vertical plane, flow convergence occurs between 9 and 11 km at the leading edge of the jet core. Above and below the convergence zone, there are three to four tilted positive/negative wave phases. These features resemble the wave packets in Fig. 1. Hence, the simplified linear model solution

reasonably agrees with the MM5 solution. Nevertheless, note that the contour intervals are only half of that in the nonlinear model MM5 solution (Fig. 1). Comparing Figs. 4c,d and Figs. 1c,d suggests that the simplified linear model underestimates by 50% the wave amplitude since the contour intervals are halved. There are also some differences in the detailed wave structure; for example, the wave bands do not extend to the anticyclonic region as in the MM5 solution (cf. Figs. 1a and 4a). The transient waves below 5 km and above 16 km in the MM5 solution are absent in the steady-state solution. Nevertheless, they are present in the early time of the linear model simulations and disappear gradually. Comparing panels in Figs. 4c,d and Figs. 1c,d suggests that the linear model also captures the ascent/descent couplet of the vertical velocity at almost the same location as in the MM5 solution. In both the linear model solution and MM5 solution, the ascent/descent couplet above is maximized at 12 km. A second ascent/descent couplet with weaker amplitude is maximized at 9 km, which also agrees with the MM5 solution. These couplets form a quadruple pattern collocated with the sum of the normalized forcing terms $G_\delta + G_\theta + G_\zeta$. Downstream of this quadruple pattern are propagating inertia–gravity waves.

The gravity wave emission from the vortex-dipole jet provides an example of spontaneous wave emission. Here we find agreement between the linear solution and the nonlinear model solution, thereby providing clear evidence that gravity waves are generated as the response to the forcing terms identified in PZ07.

c. Linear response in the full linearized model

The steady-state linear model solution in the previous subsection is obtained with the shear terms [the brace and bracket terms in Eqs. (A1.1)–(A1.5)] neglected. Here we discuss the linear response with the shear terms included in the linear model. In addition to inclusion of the shear terms, we also use the temporally varying balanced flow as the background flow. Both the forcing and background flow are obtained by inverting the balanced flow through PV inversion from the hourly output of the MM5 simulation.

Figure 5 displays the linear model simulated fields (including the horizontal divergence and the vertical velocity) when all the forcing terms F_δ , F_θ , and F_ζ (Fig. 2) are imposed. The wave response is plotted after 30 h of linear model integration from 180 h of the MM5 simulation. In general, the linear model solution, at least the general pattern, reasonably agrees with the MM5 solution in Fig. 1. Both the pattern and amplitude of the wave packet in the immediate jet exit region are close to the MM5 simulation. For example, the first wave band (from the horizontal divergence) downstream from the

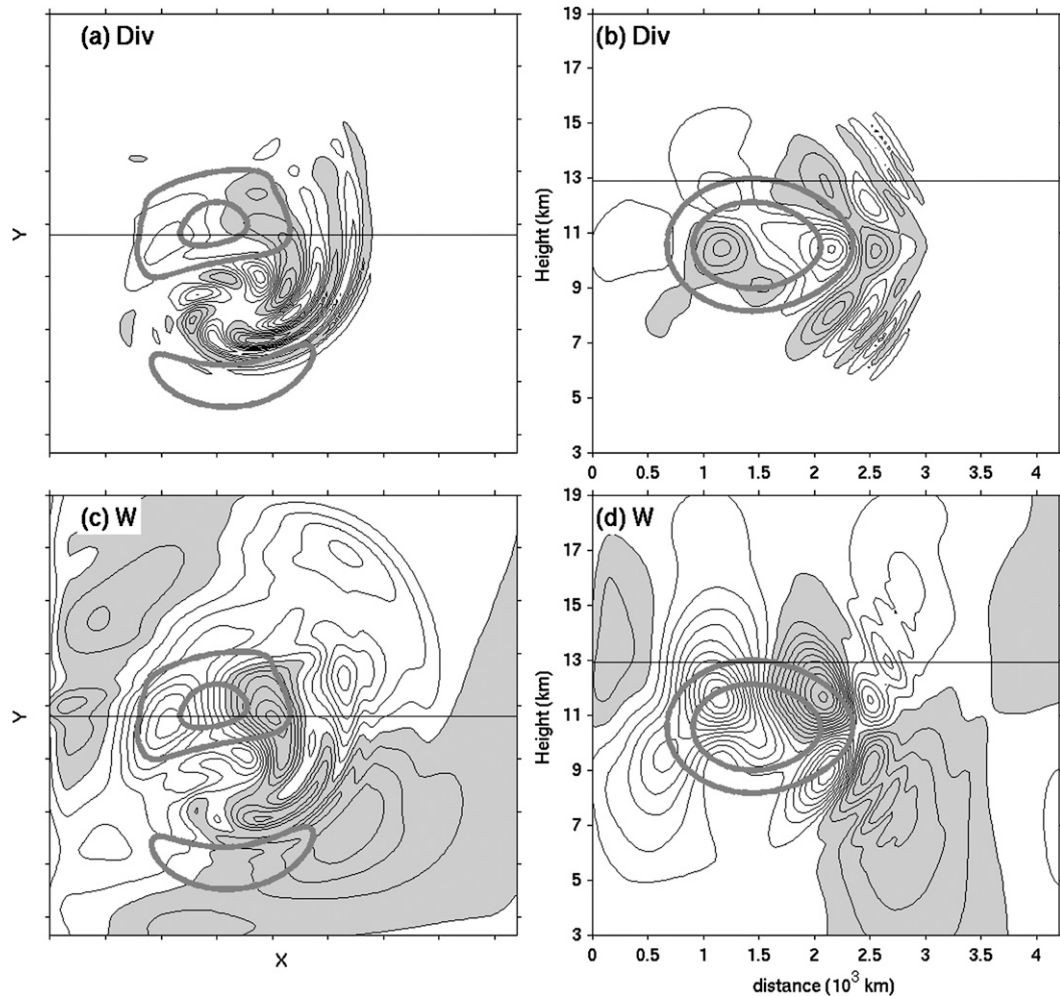


FIG. 4. As in Fig. 1 but for (a) horizontal divergence ($CI = 0.5 \times 10^{-6} \text{ s}^{-1}$) simulated by the linear model *without* the shear terms due to all the forcing terms at 12.9 km and (b) the corresponding vertical cross section. (c),(d) As in (a),(b) but for the linear model simulated vertical velocity ($CI = 2.5 \times 10^{-4} \text{ m s}^{-1}$).

jet core appears almost the same distance relative to the 20 m s^{-1} wind contour.

It should be noted that Fig. 5 shows the linear model simulated wave pattern that has the best agreement with the nonlinear model MM5 simulation in Fig. 1 because the linear response continues to grow with respect to time during the integration period. This is partly due to a possible instability mechanism associated with the shear terms in the complete linear model [Eqs. (A1.1)–(A1.5)]. This instability is indicated by the growing kinetic energy associated with rotational winds (Fig. 6), while the kinetic energy of the divergent winds remains nearly steady. Such instability is of algebraic type (as can be seen from the algebraic growth of kinetic energy of the rotational winds) and may be related to the mechanism discussed in Snyder (1999). Nevertheless, a detailed analysis of this instability is not pursued here because this instability is

not tied to the divergent wave motion and is unlikely to be related to the origins of the gravity waves.

d. Response to the individual forcing terms

Linear model solutions are also obtained by imposing the individual forcing terms F_δ , F_θ , and F_ζ using the simplified version of the linear model. Figures 7a,b show the results as F_ζ is imposed to the linear model. Both the fields near the jet core and downstream wave signals are very similar to those in Fig. 4 except that the two fields are less noisy. Linear response to each individual term of $F_\zeta = -\mathbf{U}_B \cdot \nabla \zeta_B - f\delta_B$ is also obtained. Again, the time tendency is neglected since it is very small. The spatial pattern of G_ζ with only the nonlinear advection of the balanced vorticity, $-\mathbf{U}_B \cdot \nabla \zeta_B$, is almost the same as G_ζ (Figs. 3c,d). The corresponding wave response

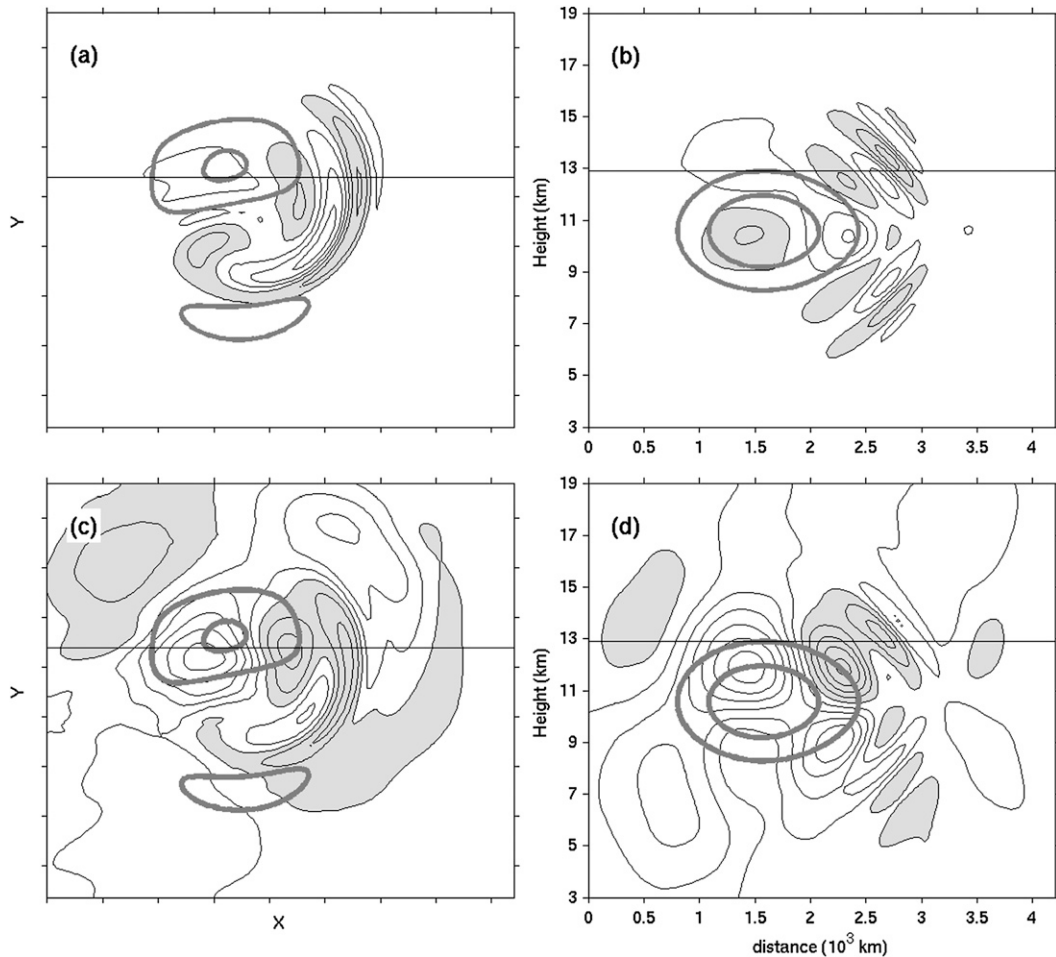


FIG. 5. Linear model simulated 30-h horizontal divergence ($CI = 10^{-6} \text{ s}^{-1}$; zero value omitted; shaded, positive) from the model with *all* the shear terms included (a) at 12.9 km and (b) the corresponding vertical cross section. (c) Vertical velocity ($CI = 5 \times 10^{-4} \text{ m s}^{-1}$; zero value omitted; shaded, positive) at 12.9 km and (d) the corresponding vertical cross section. Wind speed (thick gray) is contoured at 20, 25, and 30 m s^{-1} at 11.5 km in (a) and (c) and along the vertical cross sections in (b) and (d). The solid gray lines (left panels) indicate the cross sections (right panels). The solid gray lines (right panels) indicate the level of 12.9 km. The distance between ticks (left panels) is 500 km.

from $-\mathbf{U}_B \cdot \nabla \zeta_B$ is also almost the same as that from F_ζ . Therefore, the advection of vorticity, $-\mathbf{U}_B \cdot \nabla \zeta_B$, is mostly responsible for wave generation. This term emphasizes that the forcing is heavily weighted in the region of large wind, which is highly flow-dependent. The additional vertical derivative of this term in the normalized vorticity forcing in Eq. (4) further indicates that the spatial structure of the jet is also important for the forcing since the derivative of the background wind is involved.

Figures 7c,d and 7e,f show the linear response from the other two forcing terms, F_δ and F_θ . The linear response to F_δ and F_θ barely contains any meaningful wave signature. Specifically, the corresponding fields near the jet core (e.g., the flow convergence zone and the ascent/descent couplet) are absent and the wave solutions are

much weaker than waves forced by F_ζ with a spatial pattern inconsistent with the MMS solution. This is also consistent with the diagnosis of the normalized forcing terms G_ζ , G_δ , and G_θ (Fig. 3) since G_δ and G_θ are much smaller than G_ζ .

In summary, these simulations with different forcing terms suggest that the vorticity forcing term—in particular, the nonlinear advection of the balanced vorticity—is the leading contributor to wave generation from the localized dipole jet.

e. Wave response during the initial few hours

The linear response due to the vorticity forcing during the first inertial period is analyzed to demonstrate the underlying physical process of the wave generation in the forced linear model. This is not the same adjustment

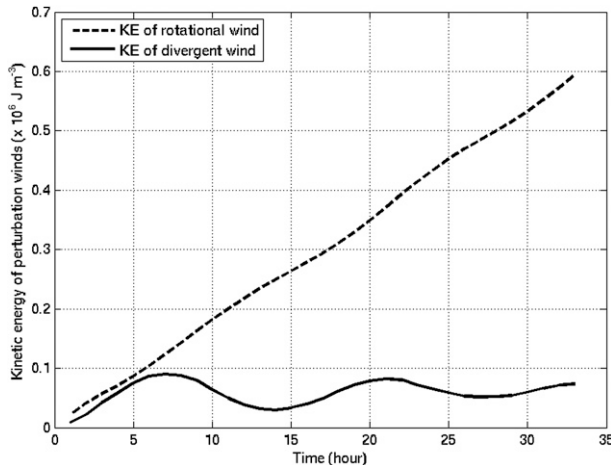


FIG. 6. Time series of total kinetic energy associated with rotational winds (dashed) and divergent winds (solid) from the linear model simulation in Fig. 5 in which all the shear terms are included.

process as that in the MM5 simulation (Wang et al. 2009), but is more as a switch-on experiment to demonstrate the role of vorticity forcing.

Figure 8 shows relative vorticity, horizontal wind divergence, and vertical velocity at hours 3, 6, and 18. As the forcing has been imposed for a few hours (3 h), negative vorticity is produced. A convergent flow (flow convergence) is associated with this negative vorticity. Continuity ensures that an upward (downward) motion appears above (below) the convergence zone near the jet core. As the amplitude of the response to the vorticity forcing increases, flow convergence and the upward/downward motion also strengthen. At hour 6 (Figs. 8d–f), a weak wave response already appears above/below the convergence zone. After one inertial period, there are wavelike motions in the divergence field. At hour 18 (Figs. 8g–i), the wave response in the divergence field shows several distinct phases, resembling the wave signature in Fig. 4b.

To understand the above evolution of the linear solution, we may consider the gradient wind balance within a coordinate whose origin is centered at the maximum of the forcing. The negative vorticity forcing produces an anticyclonic wind; because of imbalance in the radial direction, such rotational wind creates inward acceleration, driving a net inward flow. The inward flow produces a cyclonic acceleration in order to restore the gradient wind balance. This flow convergence also creates upward and downward motion because of the continuity, and waves generated as isentropes are distorted. Indeed, this is the situation in Fig. 8 during the first inertial period of the linear model simulation. Alternative to the above interpretation, the same flow evolution may also be achieved

from consideration of the balance among terms in the linearized vorticity equation [Eq. (A1.2)].

5. Sensitivity experiments

The analysis in the previous section adopts two numerical approximations: the neglect of small-scale details and the use of the quasigeostrophic vertical velocity (w_{QG}) for the calculation of the forcing in Eqs. (1) and (4). Here we discuss two additional numerical experiments: in one experiment we reduce the horizontal smoothing and in the other we neglect w . As shown below, these factors have very limited influence on the wave responses.

a. Effects of horizontal smoothing on the linear response

To evaluate the smoothing effect of the low-pass digital filter, additional experiments are performed by changing the cutoff wavelength of the digital filter. In one simulation, the cutoff wavelength is chosen to be 240 km. The forcing terms are noisy (not shown), and the spatial structure is not as clean as that in Figs. 2 and 3.

Figures 9a and 9b show the linear wave response in this run. It appears that wave amplitudes become stronger, and the general wave pattern is very similar to that discussed for Figs. 4a,b. For example, wave bands extend farther to the anticyclone in Fig. 9a. Nevertheless, the wave pattern is robust when a different smoothing filter is applied. This experiment suggests that the smoothing may cause weakening of the forcing and its wave response. This is not unexpected because it is well known that the response function to a bandpass filter may damp the power near the chosen window.

b. Response to the forcing diagnosed from different vertical velocity

As discussed before, quasigeostrophic vertical velocity (w_{QG}) is used to evaluate the forcing terms. Here w_{QG} is simply replaced with zero vertical velocity to diagnose the forcing terms. Figures 9c and 9d show the horizontal divergence obtained from the steady-state solution using the linear model. The general wave pattern shows only minor change compared to Fig. 4a. Therefore, the ad hoc use of the w_{QG} seems to have no impact on the linear model solution.

6. Wave response due to the flow imbalance under the linear framework of PZ07

The flow imbalance indicated by ΔNBE , the residual of the nonlinear balance equation, has a localized spatial structure that collocates with the jet core. It is suggested in the literature (e.g., Kaplan and Paine 1977; Zhang

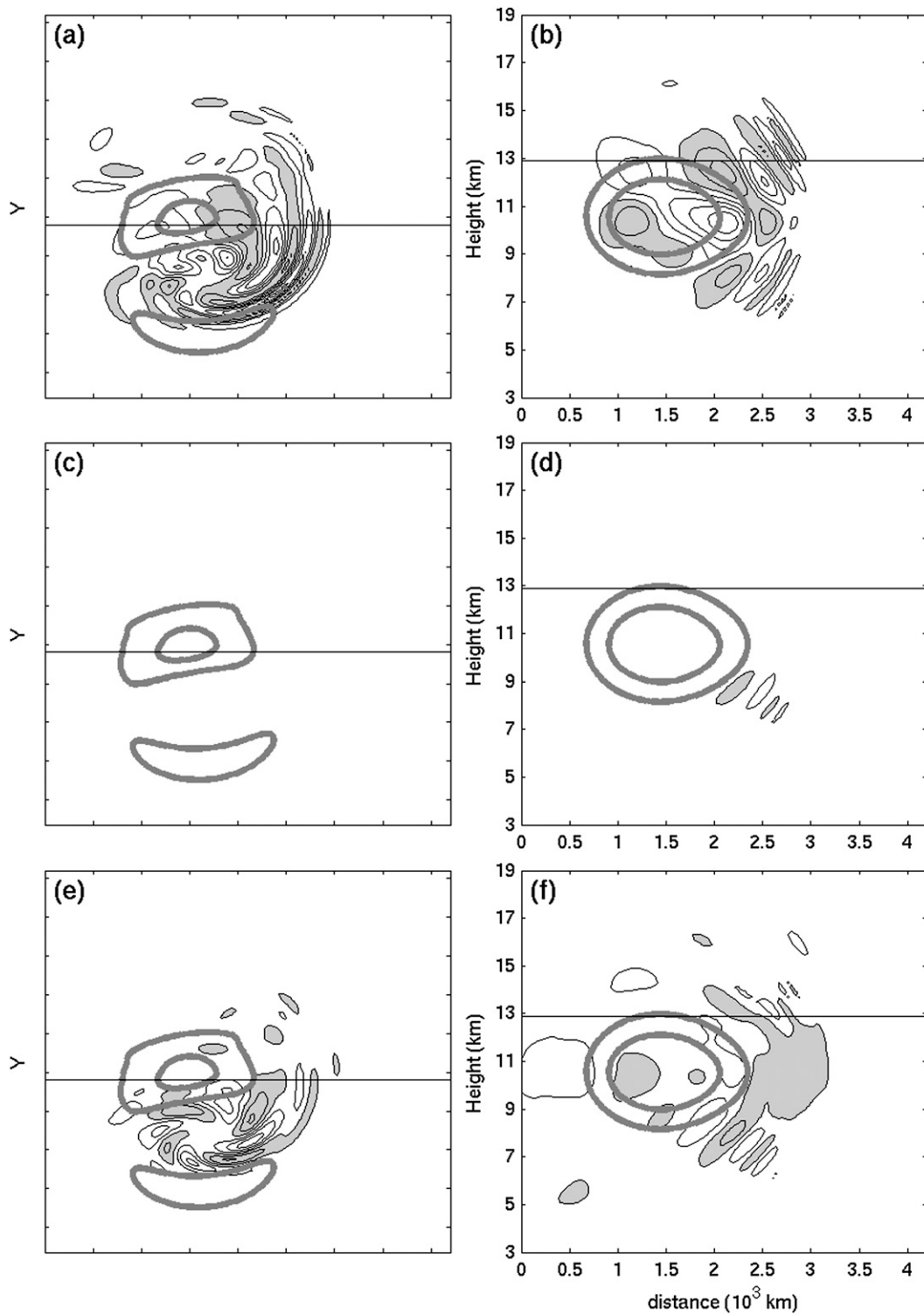


FIG. 7. (a),(b) As in Figs. 4a,b, respectively, but for the linear response due to the forcing F_c . (c),(d) As in (a),(b) but for the linear response due to the forcing term F_b . (e),(f) As in (a),(b) but for the linear response due to the forcing term F_θ .

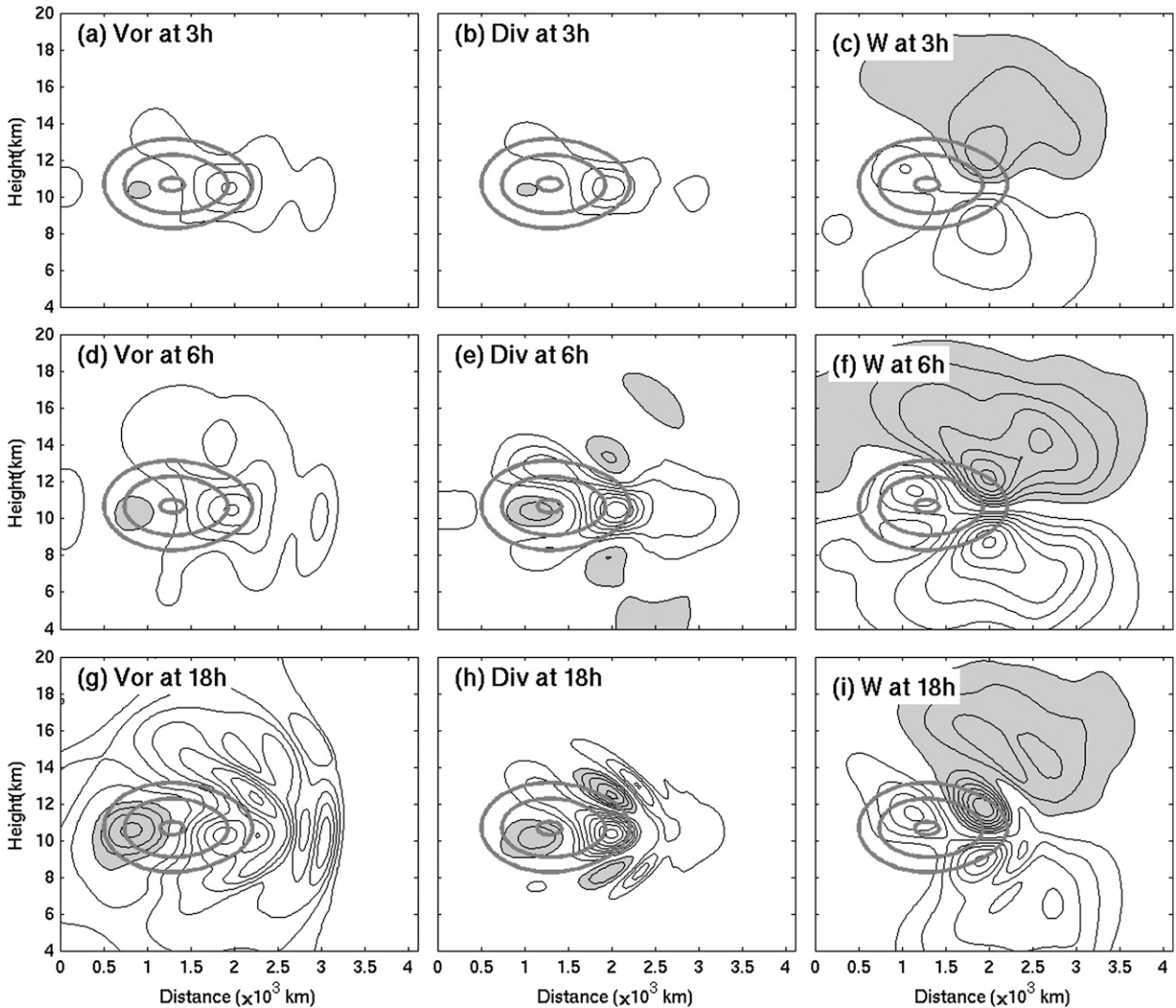


FIG. 8. Linear model-simulated (a),(d),(g) relative vorticity ($CI = 10^{-6} \text{ s}^{-1}$; zero value omitted; shaded, positive), (b),(e),(h) divergence ($CI = 0.5 \times 10^{-6} \text{ s}^{-1}$), and (c),(f),(i) vertical velocity ($CI = 2.5 \times 10^{-4} \text{ m s}^{-1}$) at 3, 6, and 18 h due to the imposed vorticity forcing along the same vertical cross section as Fig. 7b.

et al. 2000) that ΔNBE is a good indicator of flow imbalance. Past studies also suggest that ΔNBE can be used to infer the location and timing of gravity waves generated during baroclinic jet-front cycles (e.g., Zhang 2004). PZ07 expands this idea and suggests three leading terms as the forcing to the divergence, vorticity, and thermal equations. The normalized forms of these terms in PZ07 [their Eq. (15)] are written as

$$\Gamma_{\Delta NBE} = -(\partial_t + \mathbf{U} \cdot \nabla) \frac{\partial}{\partial z} [\Delta NBE],$$

$$\Gamma_{\zeta} = -f \frac{\partial}{\partial z} [-(\partial_t + \mathbf{U} \cdot \nabla)\zeta - f\delta],$$

and

$$\Gamma_{\theta} = \frac{g}{\Theta} \Delta [-(\partial_t + \mathbf{U} \cdot \nabla)\theta - w \partial_z \bar{\Theta}], \quad (5)$$

where $\Delta NBE = f\zeta - \Delta\Phi + 2J(u, v)$ and $J(u, v)$ is the Jacobian of the full horizontal wind (u, v) . These terms are the direct forcing imposed to the linearized equations. Here we evaluate them using the total flow and apply smoothing using a 2D low-pass filter with the cutoff wavelength 600 km.

Figure 10 shows the linear response to the sum of all the three terms. Similar to the wave in the MM5 solution, the wave packet extends to the cyclonic side of the dipole at 12.9 km. Also, the convergence zone is located ahead of the jet core. Above and below this convergence zone, there are wave packets propagating away, although

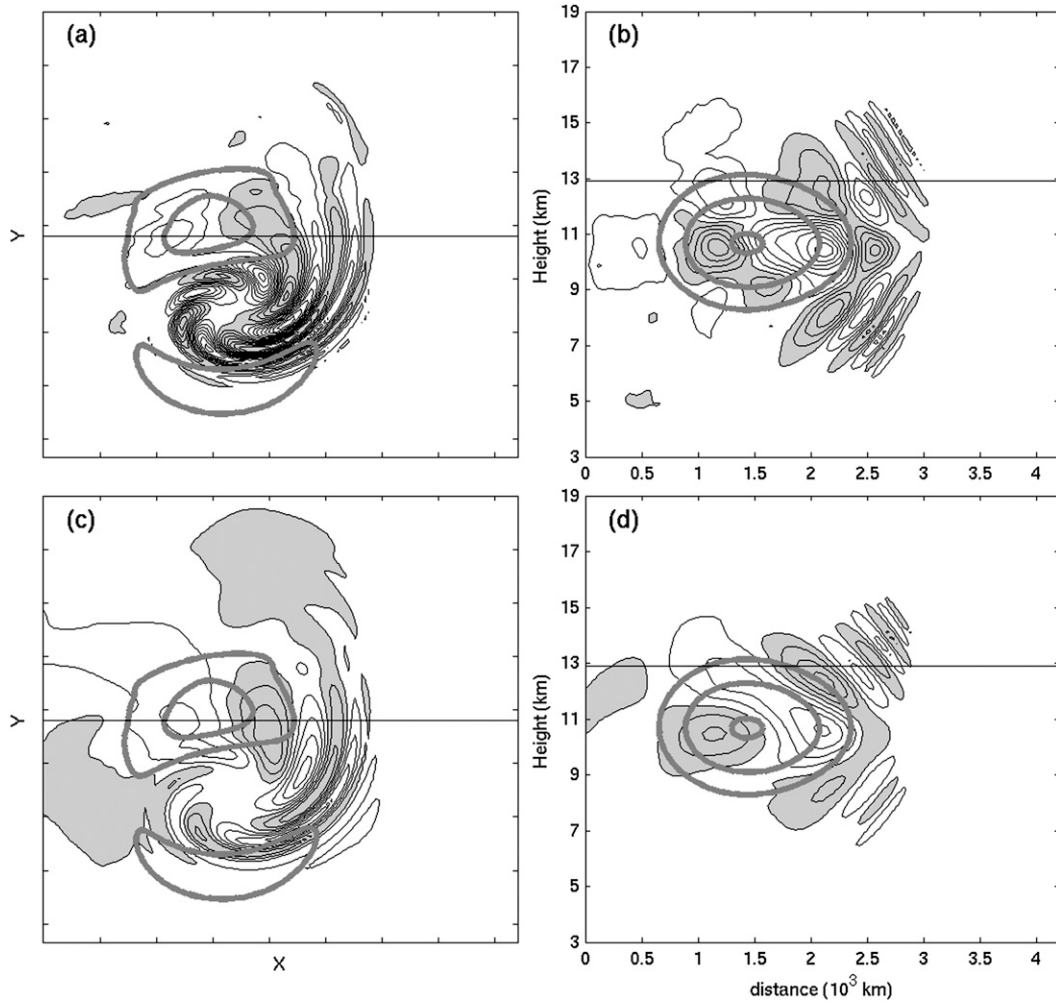


FIG. 9. (a),(b) As in Figs. 4a,b but all the forcing terms are smoothed by a 2D filter with a cutoff wavelength 240 km. (c),(d) As in (a),(b), but the linear response is from the linear model forced by the forcing terms in which zero vertical velocity is used as the background vertical velocity.

the wave field is noisier near the bottom and top boundaries, possibly due to wave reflection.

On the other hand, it is of interest to study the wave response to the flow imbalance only due to the residual of nonlinear balance equation (ΔNBE , the leading term in the divergence forcing of PZ07) using the linear model. Here we impose the ΔNBE forcing but evaluate it using the total flow output from the MM5 simulation instead of using the nonlinearly balanced flow, as for Fig. 4 and in Eq. (2).

Figure 11 shows the horizontal and vertical distribution of ΔNBE , the normalized ΔNBE forcing term $\Gamma_{\Delta\text{NBE}}$, and the linear response to ΔNBE . Distinct gravity wave packets appear in the forced response (Figs. 11e,f) in a similar location but with only half of the amplitude as in the MM5 solution (Fig. 1). Moreover, the forced waves

have almost a reversed phase compared to those in the MM5 solution. The difference between these two solutions is even more pronounced in the vertical velocity fields (not shown). Despite these differences, the general wave pattern from the horizontal divergence is still similar to the MM5 solution if these fields are plotted with reversed sign.

The phase bias in the ΔNBE forced solution is due to the dominance of the vorticity term in ΔNBE . In fact, there is cancellation between the vorticity term in ΔNBE and the vorticity term in Γ_{ζ} in Eq. (5). We also compute the wave response due to the reduced ΔNBE forcing, defined as $-\Delta\Phi + 2J(u, v)$ with only the pressure and Jacobian terms included. The linear response to $-\Delta\Phi + 2J(u, v)$ is the same as that in Fig. 10 (not shown), suggesting that the sum of $\Gamma_{\Delta\text{NBE}}$, Γ_{θ} , and Γ_{ζ} in Eq. (5) approximates to the normalized form of $-\Delta\Phi + 2J(u, v)$.

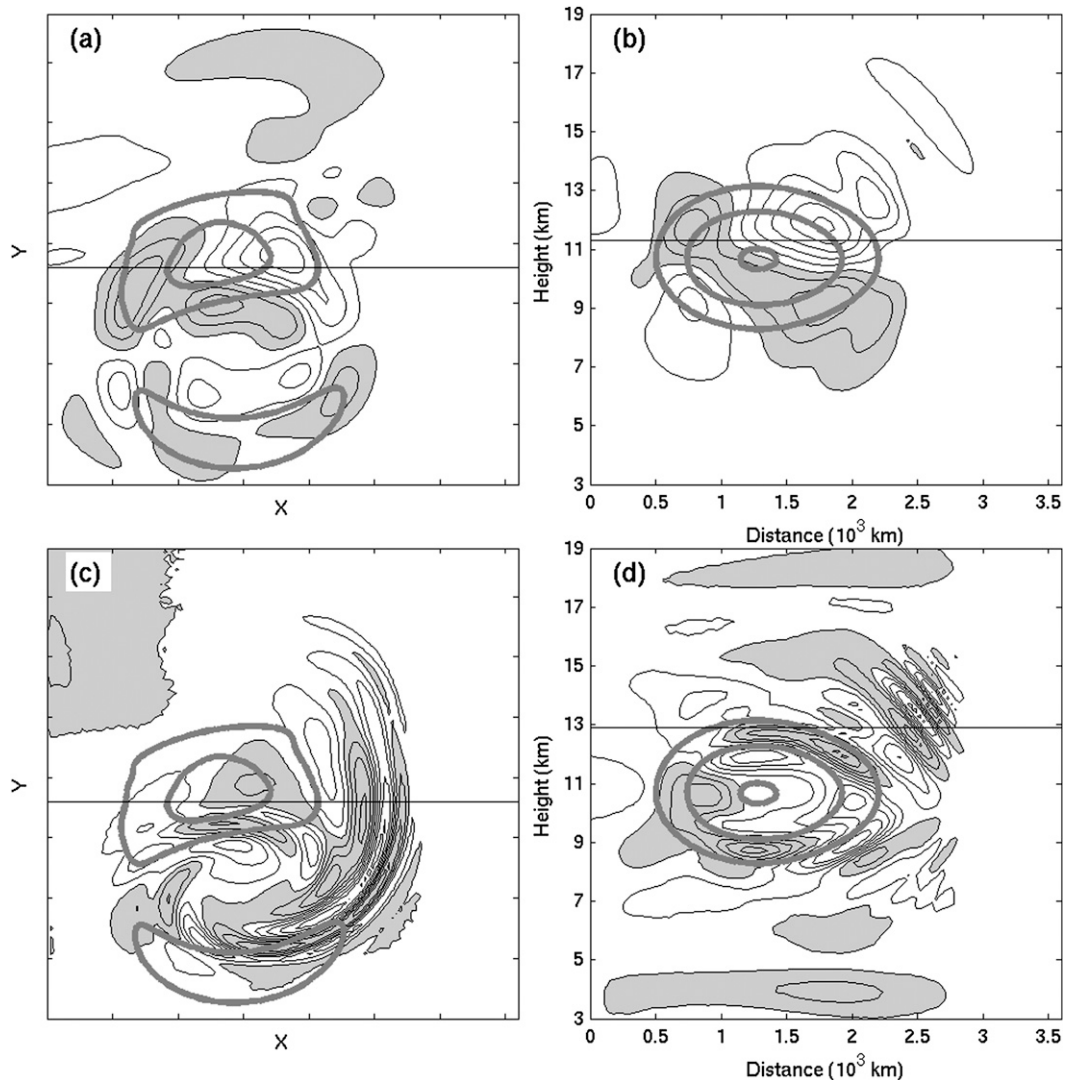


FIG. 10. The total normalized forcing ($\Gamma_{\Delta NBE} + \Gamma_{\zeta} + \Gamma_{\theta}$) evaluated using the total flow ($CI = 0.005 \times 10^{-8} \text{ s}^{-2}$; zero value omitted; shaded is positive) (a) at 11.5 km and (b) the corresponding vertical cross section. The linear model simulated horizontal divergence due to the forcing evaluated using the total flow is plotted (c) at 12.9 km and (d) the corresponding vertical cross section. Wind speed (thick gray) is contoured at 20, 25, and 30 m s^{-1} at 11.5 km in (a) and (c) and along the vertical cross sections in (b) and (d). The solid gray lines (left panels) indicate the cross sections (right panels). The solid gray lines indicate the level of (b) 11.3 and (d) 12.9 km. Distance between ticks (left panels) is 500 km.

In other words, within the vortex-dipole jet the normalized vorticity forcing G_{ζ} , instead of $\Gamma_{\Delta NBE}$, is also found to be the leading contributor to the generation of the jet-exit-region gravity waves under the linear framework of PZ07 as in Eq. (5).

In summary, this section demonstrates that the gravity waves can be forced similarly by the leading terms identified in Eq. (15) of PZ07 [as reproduced in Eq. (5)]. However, owing to apparent cancellation between different forcing terms and the ambiguity in separating the imbalance from large-scale background flow in PZ07,

there is an inherent limitation in attributing the wave response to individual forcing terms.

7. Summary and discussion

This study investigates the source mechanism of gravity waves from a localized jet within a midlevel vortex dipole using a linear model, which was formulated by PZ07. Three types of forcings are imposed on the linear model. Different from PZ07, we explicitly separate the flow into the balanced state and an unbalanced part of small amplitude. The potential vorticity inversion

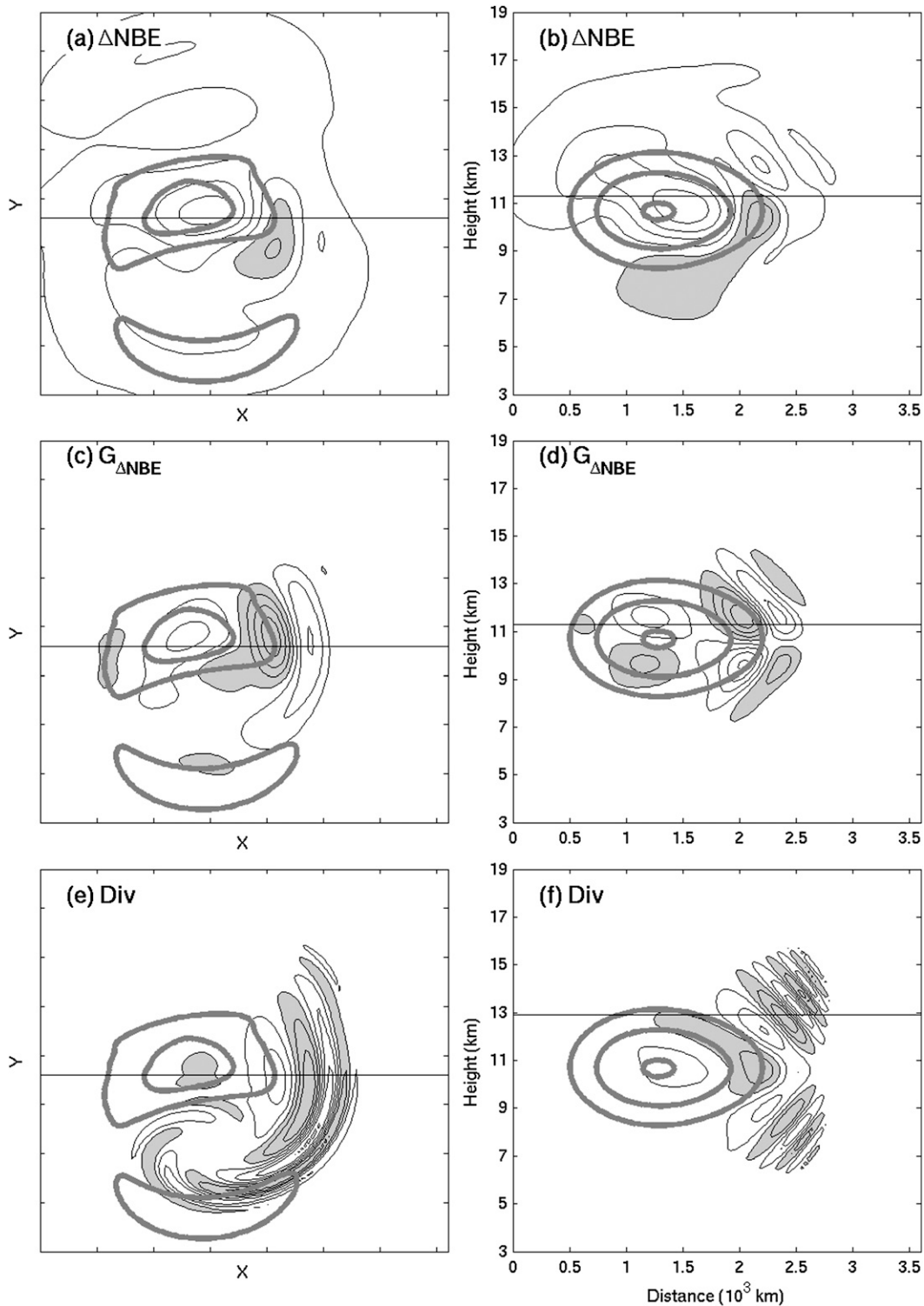


FIG. 11. ΔNBE ($\text{CI} = 0.005 \times 10^{-8} \text{ s}^{-2}$; zero value omitted; shaded, positive) evaluated using the total flow from MM5 valid at 210 h (a) at 11.3 km and (b) the corresponding vertical cross section; $\Gamma_{\Delta\text{NBE}}$ ($\text{CI} = 0.05 \times 10^{-16} \text{ m}^{-1} \text{ s}^{-3}$; zero value omitted; shaded, positive) (c) at 11.5 km and (d) the corresponding vertical cross section. The linear model-simulated horizontal divergence due to the ΔNBE forcing (e) at 12.9 km and (f) the corresponding vertical cross section. Wind speed (thick gray) is contoured at 20, 25, and 30 m s^{-1} at 11.5 km in (a),(c), and (e) and along the vertical cross section in (b),(d), and (f). The solid gray lines (right panels) indicate the level of (b),(d) 11.3 km and (f) 12.9 km. Distance between ticks (left panels) is 500 km.

constrained by the nonlinear balance is used to obtain the balanced flow. The linear model is used to obtain steady wave solutions by imposing all of the diagnosed forcings. The linear solution of the gravity wave packets from the localized jet is in reasonable agreement with the MM5 solution, thereby providing evidence to support the effectiveness of the revised formulation of spontaneous wave generation proposed in PZ07.

The significance of this analysis rests in that this is a clear demonstration of spontaneous wave generation from a quasi-balanced flow following linear dynamics. Our analysis complements findings from Snyder et al. (2009) that gravity waves spontaneously emitted in the exit region of the dipole jet are a forced, linear response. Different from Snyder et al. (2009), we employ potential vorticity inversion to obtain the balanced flow to avoid the systematic bias in the QG dynamic relative to the fully nonlinear dynamics. We further compare different wave sources and find that the vorticity forcing is the largest among different forcing terms. Results from the linear model simulations further reveal that the vorticity forcing is the leading contributor to gravity waves in the jet exit region. An instability is also found in linear simulations with all shear terms included. Nevertheless, such instability is absent in simulations without the shear terms. Therefore, the source of linear instability comes from the background shear terms in the wave operator. This further demonstrates that gravity waves from the vortex dipole are not tied to the instability mechanism that may be inherent in the linear model, consistent with Viúdez (2007). Our study also complements that of Viúdez in that we develop a more systematic approach to recover the wave solutions in the linear model.

Nevertheless, we do not intend to generalize our conclusions on the importance of the vorticity forcing beyond the quasi-steady vortex-dipole jets. Instead, the importance of different forcing terms is likely flow dependent. In fact, using the same linear framework under the nonlinearly balanced background state, we do not find that the vorticity forcing is the leading contributor to gravity wave generation during the idealized baroclinic jet-front cycles simulated in Zhang (2004), which will be reported in a separated study.

Based on the wave forcing diagnosis and the linear model solutions, the effect of the localized jet on the wave generation may be summarized: the horizontal advection of the localized jet is essential because the forcing is heavily weighted near the region of local wind maximum in the *advection operator*; also, the inclusion of wind in the linear wave operator allows waves to be refracted as in the nonlinear simulations.

Under the same linear model framework, we also demonstrate that gravity waves can be forced similarly by

the leading terms of large-scale flow imbalance identified in Eq. (15) in PZ07. However, owing to apparent cancellation between different forcing terms and the ambiguity in separating imbalance from large-scale background flow formulated in PZ07, there is an inherent limitation in attributing wave response to individual forcing terms.

Acknowledgments. This research was completed as part of S. Wang's doctoral dissertation at Texas A&M University. The authors are thankful to Chris Davis for the PV inversion codes. The authors are grateful to Chris Snyder, Craig Epifanio, and Riwal Plougonven for discussions beneficial to this study and to two anonymous reviewers for their insightful comments. The research was supported by NSF Grants ATM-0203238, ATM-0618662, and ATM-0904635.

APPENDIX

Formulation of the Linear Model

Similar to PZ07, we first separate wind components (u, v, w), potential temperature θ , and Boussinesq disturbance pressure Φ into the large-scale (background) component and the perturbation component: $u = u_B + u', v = v_B + v', w = w_B + w', \theta = \theta_B + \theta', \Phi = \Phi_B + \Phi'$, and $\mathbf{U}_B = (u_B, v_B, w_B)$, $\mathbf{U} = (u', v', w')$. The linearized equation set in the compressible nonhydrostatic flow is written, with the primes dropped, as

$$\frac{\partial \delta}{\partial t} + \mathbf{U}_B \cdot \nabla \delta + \left[\left(\frac{\partial}{\partial x} \mathbf{U}_B \right) \cdot \nabla u + \left(\frac{\partial}{\partial y} \mathbf{U}_B \right) \cdot \nabla v \right] + \{ \mathbf{V}_H \cdot (\mathbf{U} \cdot \nabla \mathbf{U}_B) \} - f \zeta + \Delta \Phi = F_\delta, \quad (\text{A1.1})$$

$$\frac{\partial \zeta}{\partial t} + \mathbf{U}_B \cdot \nabla \zeta + \left[- \left(\frac{\partial}{\partial y} \mathbf{U}_B \right) \cdot \nabla u + \left(\frac{\partial}{\partial x} \mathbf{U}_B \right) \cdot \nabla v \right] + \{ \mathbf{k} \cdot \nabla \times (\mathbf{U} \cdot \nabla \mathbf{U}_B) \} + f \delta = F_\zeta, \quad (\text{A1.2})$$

$$\frac{\partial \theta}{\partial t} + \mathbf{U}_B \cdot \nabla \theta + \left\{ u \frac{\partial \theta_B}{\partial x} + v \frac{\partial \theta_B}{\partial y} \right\} + w \frac{\partial \theta_B}{\partial z} = F_\theta, \quad (\text{A1.3})$$

$$\frac{\partial w}{\partial t} + \mathbf{U}_B \cdot \nabla w + \{ \mathbf{U} \cdot \nabla (w_B) \} = -\Phi_z + \frac{g}{\Theta} \theta, \quad (\text{A1.4})$$

$$\frac{\partial_t \Phi}{\partial t} = -C_s^2 \nabla \mathbf{U}. \quad (\text{A1.5})$$

Here \mathbf{k} is the vertical unit vector, f the Coriolis parameter, and C_s the sound speed (300 m s^{-1}). The momentum forcings F_u and F_v , the thermal forcing F_θ , the divergence forcing F_δ , and the vorticity forcing term F_ζ are given in Eq. (1).

The linear model equation set has five prognostic variables: horizontal divergence, relative vorticity, vertical velocity, potential temperature, and Boussinesq disturbance pressure. The linearized equation set (A1.1)–(A1.5) is closed by the diagnostic relation of the perturbation winds, which are obtained via Helmholtz decomposition $\mathbf{u} = \nabla\phi - \mathbf{k} \times \nabla\psi$, where the potential ϕ and streamfunction ψ are related to divergence and vorticity:

$$\delta = \nabla^2\phi; \quad \zeta = \nabla^2\psi. \quad (\text{A2})$$

These equations are solved with periodic boundary conditions, which are chosen based on the fact that the disturbance of interest stays away from the lateral boundaries.

The terms in the braces in (A1.1)–(A1.5) denote the terms associated with the horizontal and vertical derivatives of the background winds, while the brackets denote the additional terms present in the u , v wind-based linear model. Here all of these terms are named *shear terms* for our convenience.

REFERENCES

- Blumen, W., 1972: Geostrophic adjustment. *Rev. Geophys.*, **10**, 485–528.
- Cahn, A., 1945: An investigation of the free oscillations of a simple current system. *Mon. Wea. Rev.*, **2**, 113–119.
- Davis, C. A., and K. A. Emanuel, 1991: Potential vorticity diagnostics of cyclogenesis. *Mon. Wea. Rev.*, **119**, 1929–1953.
- Ford, R., 1994: Gravity wave radiation from vortex trains in rotating shallow water. *J. Fluid Mech.*, **281**, 81–118.
- , M. E. McIntyre, and W. A. Norton, 2000: Balance and the slow quasimanifold: Some explicit results. *J. Atmos. Sci.*, **57**, 1236–1254.
- Fritts, D. C., and Z. Luo, 1992: Gravity wave excitation by geostrophic adjustment of the jet stream. Part I: Two-dimensional forcing. *J. Atmos. Sci.*, **49**, 681–697.
- Gent, P. R., and J. C. McWilliams, 1982: Intermediate model solutions to the Lorenz equations: Strange attractors and other phenomena. *J. Atmos. Sci.*, **39**, 3–13.
- Hertzog, A., C. Souprayen, and A. Hauchecorne, 2001: Observation and backward trajectory of an inertia-gravity wave in the lower stratosphere. *Ann. Geophys.*, **19**, 1141–1155.
- Kaplan, M. L., and D. A. Paine, 1977: The observed divergence of the horizontal velocity field and pressure gradient force at the mesoscale. Its implications for the parameterization of three-dimensional momentum transport in synoptic-scale numerical models. *Beitr. Phys. Atmos.*, **50**, 321–330.
- Klemp, J. B., and R. B. Wilhelmson, 1978: The simulation of three-dimensional convective storm dynamics. *J. Atmos. Sci.*, **35**, 1070–1096.
- Koch, S. E., and P. B. Dorian, 1988: A mesoscale gravity wave event observed during CCOPE. Part III: Wave environment and probable source mechanisms. *Mon. Wea. Rev.*, **116**, 2570–2592.
- , and Coauthors, 2005: Turbulence and gravity waves within an upper-level front. *J. Atmos. Sci.*, **62**, 3885–3908.
- Luo, Z., and D. C. Fritts, 1993: Gravity-wave excitation by geostrophic adjustment of the jet stream. Part II: Three-dimensional forcing. *J. Atmos. Sci.*, **50**, 104–115.
- Marks, C. J., and S. D. Eckermann, 1995: A three-dimensional nonhydrostatic ray-tracing model for gravity waves: Formulation and preliminary results for the middle atmosphere. *J. Atmos. Sci.*, **52**, 1959–1984.
- McIntyre, M. E., 2009: Spontaneous imbalance and hybrid vortex-gravity structures. *J. Atmos. Sci.*, **66**, 1315–1326.
- O’Sullivan, D., and T. J. Dunkerton, 1995: Generation of inertia-gravity waves in a simulated life cycle of baroclinic instability. *J. Atmos. Sci.*, **52**, 3695–3716.
- Plougonven, R., and H. Teitelbaum, 2003: Comparison of a large-scale inertia-gravity wave as seen in the ECMWF analyses and from radiosondes. *Geophys. Res. Lett.*, **30**, 1954, doi:10.1029/2003GL017716.
- , and C. Snyder, 2007: Inertia-gravity waves spontaneously generated by jets and fronts. Part I: Different baroclinic life cycles. *J. Atmos. Sci.*, **64**, 2502–2520.
- , and F. Zhang, 2007: On the forcing of inertia-gravity waves by synoptic-scale flows. *J. Atmos. Sci.*, **64**, 1737–1742.
- , H. Teitelbaum, and V. Zeitlin, 2003: Inertia gravity wave generation by the tropospheric midlatitude jet as given by the Fronts and Atlantic Storm-Track Experiment radio soundings. *J. Geophys. Res.*, **108**, 4686, doi:10.1029/2003JD003535.
- , C. Snyder, and F. Zhang, 2009: Comments on “Application of the Lighthill–Ford theory of spontaneous imbalance to clear-air turbulence forecasting.” *J. Atmos. Sci.*, **66**, 2506–2510.
- Rosby, C., 1938: On the mutual adjustment of pressure and velocity distributions in certain simple current systems, 2. *J. Mar. Res.*, **1**, 239–263.
- Schneider, R. S., 1990: Large-amplitude mesoscale wave disturbances within the intense Midwest extratropical cyclone of 15 December 1987. *Wea. Forecasting*, **5**, 533–558.
- Skamarock, W. C., and J. B. Klemp, 1992: The stability of time-split numerical methods for the hydrostatic and the nonhydrostatic elastic equations. *Mon. Wea. Rev.*, **120**, 2109–2127.
- Snyder, C., 1999: Error growth in flows with finite-amplitude waves or coherent structures. *J. Atmos. Sci.*, **56**, 500–506.
- , W. C. Skamarock, and R. Rotunno, 1993: Frontal dynamics near and following frontal collapse. *J. Atmos. Sci.*, **50**, 3194–3212.
- , D. J. Muraki, R. Plougonven, and F. Zhang, 2007: Inertia-gravity waves generated within a dipole vortex. *J. Atmos. Sci.*, **64**, 4417–4431.
- , R. Plougonven, and D. Muraki, 2009: Mechanisms for spontaneous gravity-wave generation within a dipole vortex. *J. Atmos. Sci.*, **66**, 3464–3478.
- Uccellini, L. W., and S. E. Koch, 1987: The synoptic setting and possible source mechanisms for mesoscale gravity wave events. *Mon. Wea. Rev.*, **115**, 721–729.
- Van Tuyl, A. H., and J. A. Young, 1982: Numerical simulation of nonlinear jet streak adjustment. *Mon. Wea. Rev.*, **110**, 2038–2054.
- Viúdez, A., 2006: Spiral patterns of inertia-gravity waves in geophysical flows. *J. Fluid Mech.*, **562**, 73–82.
- , 2007: The origin of the stationary frontal wave packet spontaneously generated in rotating stratified vortex dipoles. *J. Fluid Mech.*, **593**, 359–383.
- , 2008: The stationary frontal wave packet spontaneously generated in mesoscale dipoles. *J. Phys. Oceanogr.*, **38**, 243–256.

- Wang, S., and F. Zhang, 2007: Sensitivity of mesoscale gravity waves to the baroclinicity of jet-front systems. *Mon. Wea. Rev.*, **135**, 670–688.
- , —, and C. Snyder, 2009: Generation and propagation of inertia–gravity waves from vortex dipoles and jets. *J. Atmos. Sci.*, **66**, 1294–1314.
- Wicker, L. J., and W. C. Skamarock, 2002: Time-splitting methods for elastic models using forward time schemes. *Mon. Wea. Rev.*, **130**, 2088–2097.
- Wu, D. L., and F. Zhang, 2004: A study of mesoscale gravity waves over the North Atlantic with satellite observations and a mesoscale model. *J. Geophys. Res.*, **109**, D22104, doi:10.1029/2004JD005090.
- Zhang, F., 2004: Generation of mesoscale gravity waves in the upper-tropospheric jet–front systems. *J. Atmos. Sci.*, **61**, 440–457.
- , S. E. Koch, C. A. Davis, and M. L. Kaplan, 2000: A survey of unbalanced flow diagnostics and their application. *Adv. Atmos. Sci.*, **17**, 165–183.
- , —, —, and —, 2001: Wavelet analysis and the governing dynamics of a large-amplitude mesoscale gravity-wave event along the east coast of the United States. *Quart. J. Roy. Meteor. Soc.*, **127**, 2209–2245.